

Los Angeles trace
gas distributions
from a mountaintop
site

D. Fu et al.

Near-infrared remote sensing of Los Angeles trace gas distributions from a mountaintop site

D. Fu^{1,2}, T. J. Pongetti¹, J.-F. L. Blavier¹, T. J. Crawford¹, K. S. Manatt¹,
G. C. Toon¹, K. W. Wong¹, and S. P. Sander^{1,2}

¹NASA Jet Propulsion Laboratory, California Institute of Technology, Pasadena, CA 91109, USA

²UCLA Joint Institute for Regional Earth System Science and Engineering, University of California, Los Angeles, CA 90095, USA

Received: 16 September 2013 – Accepted: 16 September 2013 – Published: 7 October 2013

Correspondence to: D. Fu (dejian.fu@jpl.nasa.gov)

Published by Copernicus Publications on behalf of the European Geosciences Union.

Title Page

Abstract

Introduction

Conclusions

References

Tables

Figures

⏪

⏩

◀

▶

Back

Close

Full Screen / Esc

Printer-friendly Version

Interactive Discussion

Abstract

The Los Angeles basin is a significant anthropogenic source of major greenhouse gases (CO_2 and CH_4) and the pollutant CO , contributing significantly to regional and global climate change. We present a novel approach for monitoring the spatial and temporal distributions of greenhouse gases in the Los Angeles basin using a high-resolution spectroscopic remote sensing technique. A new Fourier Transform Spectrometer called CLARS-FTS has been deployed since May 2010 at JPL's California Laboratory for Atmospheric Remote Sensing (CLARS) on Mt. Wilson, California for automated long-term measurements of greenhouse gases. The instrument design and performance of CLARS-FTS are presented. From its mountaintop location at an altitude of 1673 m, the instrument points at a programmed sequence of ground target locations in the Los Angeles basin, recording spectra of reflected near-IR solar radiation. Column-averaged dry-air mole fractions of greenhouse gases (XGHG) including XCO_2 , XCH_4 , and XCO are retrieved several times per day for each target. Spectra from a local Spectralon[®] scattering plate are also recorded to determine background (free tropospheric) column abundances above the site. Comparisons between measurements from LA basin targets and the Spectralon[®] plate provide estimates of the boundary layer partial column abundances of the measured species. Algorithms are described for transforming the measured interferograms into spectra, and for deriving column abundances from the spectra along with estimates of the measurement precision and accuracy. The CLARS GHG measurements provide a means to infer relative, and possibly absolute, GHG emissions.

1 Introduction

The Los Angeles basin is a very large anthropogenic source of the important greenhouse gases CO_2 and CH_4 , which contribute significantly to regional and global climate change (Hoornweg, 2010). Recent legislation in California, the California Global

AMTD

6, 8807–8854, 2013

Los Angeles trace gas distributions from a mountaintop site

D. Fu et al.

Title Page

Abstract

Introduction

Conclusions

References

Tables

Figures

⏪

⏩

◀

▶

Back

Close

Full Screen / Esc

Printer-friendly Version

Interactive Discussion



Los Angeles trace gas distributions from a mountaintop site

D. Fu et al.

Title Page

Abstract

Introduction

Conclusions

References

Tables

Figures

◀

▶

◀

▶

Back

Close

Full Screen / Esc

Printer-friendly Version

Interactive Discussion

The fixed cube-corner mirror is mounted on an x - y - z translation stage. To align the two cube-corner mirrors, the fold mirrors of the metrology laser beam and the translation stage were adjusted alternately until the amplitude of the He:Ne interferogram achieved a maximum that was independent of the optical path difference.

The field stop assembly was mounted on an x - y - z translation stage. To locate the field stop in a plane perpendicular to the CLARS-FTS optical axis, a plane mirror was mounted on the field stop holder and adjusted for best autocollimation of the He:Ne beam. The pointing system directed sunlight reflected from a known LA basin landmark into the FTS. The translation stage was aligned in the z (focus) axis to achieve the best focus of the landmark image on the field stop. The field stop was then adjusted in the x - y plane perpendicular to the optical axis to center the He:Ne beam on the field stop. To verify the proper alignment of the cube corners and field stop, interferograms were recorded using a $1.2\ \mu\text{m}$ single-frequency external cavity diode laser which scattered off a diffuser plate at the entrance aperture of the FTS. Finally, using a broad-band quartz-halogen light source coupled to a collimator, spectra were recorded using an HCl gas cell. As discussed in Sect. 2.2.4, these spectra were inverted to provide information on the instrument line shape function.

2.2.2 Signal chain

Two channels are employed in the interferometer signal chain; one for the IR detector and the other for the reference laser detector. The IR channel consists of a wavelength range extended Indium Gallium Arsenide (InGaAs) photodiode detector, a variable gain transimpedance pre-amplifier, a 24-bit sigma-delta analog-to-digital converter (ADC) and a PC data acquisition computer running under LabVIEW. The InGaAs detector is thermoelectrically cooled to 190 K with an active area of 2 mm and spectral range from 0.7 to $2.5\ \mu\text{m}$. The laser metrology channel consists of a variable gain silicon photoreceiver coupled to a second channel of the ADC. The two ADC channels are sampled simultaneously.

2.2.3 Interferogram sampling methodology

CLARS-FTS uses the method of uniform time sampling (UTS) in which the IR and reference laser interferograms are recorded in equal time increments (Brasunas and Cushman, 1997; Manning and Combs, 1999; Campbell, 2008) then re-sampled into equal optical path difference increments in a post-processing step. The post-processing algorithm detects variations of the mirror velocity using the laser interferogram, computes actual optical path difference for each data point that was recorded with a constant time interval, and re-samples the white light interferograms from the time-domain to the path difference domain (Brault, 1996; Griesmann et al., 1999; Pougatchev et al., 2000). The UTS method has a number of advantages over the conventional sampling scheme that uses zero-crossings of the laser interferogram to trigger the digitization of the IR interferogram: (1) digitization at a constant sampling frequency permits the use of delta-sigma ADCs with very high resolution digitizers (24-bit), which are well-suited to the high dynamic range requirements for digitization of IR interferograms; (2) oversampling and digital filtering by the delta-sigma ADC eliminate compensation required for differential group delay between the IR and laser signal channels; (3) oversampling extends the optical frequency range into the visible and near-UV spectral regions. The post-processing algorithm, which converts CLARS-FTS interferograms to spectra, is described in Sect. 4.1.

2.2.4 Characterization of the CLARS-FTS instrument line shape

To accurately derive the mixing ratios of atmospheric trace gases from measured spectra, it is necessary to take into account the instrument line shape (ILS) function of the spectrometer, defined as the instrument's output response to a purely monochromatic input (Davis et al., 2001; Griffiths et al., 2007). For an ideal Fourier transform spectrometer, the theoretical instrument line shape function (ILS) in the frequency domain (Eq. 1) is a sinc function convolved with a rectangular function (Connes, 1961)

$$\text{ILS}(\nu) = \text{SINC}(\nu, \Delta x) \otimes \text{RECT}(\nu, \nu_0, \theta) \quad (1)$$

where,

$$\text{SINC}(\nu, \Delta x) \equiv \frac{\sin(2\pi\nu\Delta x)}{2\pi\nu\Delta x}; \quad \text{RECT}(\nu, \nu_0, \theta) \equiv \begin{cases} 1 & \text{if } -0.5\nu_0\theta^2 \leq \nu \leq 0 \\ 0 & \text{otherwise} \end{cases};$$

Δx is the optical path difference; ν and ν_0 (in cm^{-1}) are two adjacent frequencies to be distinguished; θ is the angular radius of the circular internal field of view (FOV).

The sinc function accounts for the finite optical path difference of an FTS while the rectangular function accounts for the field stop size.

To characterize the ILS, the FTS was configured using the external lamp. The experimental setup is shown in the bottom panel of Fig. 1. A gas cell containing HCl vapor (length = 9.96 cm, pressure = 5.107 hPa, temperature = 300 K, calcium fluoride (CaF_2) wedged windows) was inserted into the collimated beam path before the detector. When conducting daily atmospheric measurements, the gas cell was removed from the collimated beam to avoid signal attenuation. The absorption spectra of the HCl gas cell were recorded using CLARS-FTS ($\Delta x = 27.2$ cm, $\nu_0 = 5765\text{cm}^{-1}$, $\theta = 2.632$ mrad, with a circular field stop of 1.6 mm in diameter). The LINEFIT program (Hase et al., 1999) was applied to simulate HCl absorption spectra (top panel of Fig. 2) and retrieve the ILS (bottom plot of Fig. 2) from the observed spectral line shape. As shown in Fig. 2, the residuals in the spectral domain are essentially random. The root-mean-square of the spectral fitting residuals is about 0.08 % of the transmitted radiance and matches the estimated spectral SNR (1300 : 1) of the gas cell spectra for 10 min of integration. Equation (1) was applied to compute the theoretical ILS using the CLARS-FTS parameters. The bottom panel of Fig. 2 presents the measured (black curve) and theoretical (blue curve) ILS functions. The agreement indicates that the instrument was well aligned when these measurements were taken. Additional diagnostics include imaging of the Haidinger fringes at the field stop when the FTS is illuminated by scattered light from a beam-expanded He:Ne laser, and recordings of the ILS from a near-IR external cavity (single frequency) diode laser. Diagnostics such as this are performed seasonally to verify the alignment quality and stability.

Los Angeles trace gas distributions from a mountaintop site

D. Fu et al.

Title Page

Abstract

Introduction

Conclusions

References

Tables

Figures



Back

Close

Full Screen / Esc

Printer-friendly Version

Interactive Discussion



2.3 Pointing calibration

Accurate pointing knowledge of the instrument field of view is necessary for proper geolocation of the retrieved slant column abundances, and setup of the radiative transfer model used to fit the observed spectra. The intrinsic accuracy and repeatability of the pointing mirror gimbal are on the order of a hundredth of the CLARS-FTS instrument FOV. However, additional pointing errors arise from gimbal tilt and minor position-dependent flexing of the pointing system structure. A calibration procedure was devised to relate the readings of the pointing system encoders to the geolocated centroid of the instrument FOV.

Initially, a tracking camera, permanently mounted on the pointing system truss, was co-boresighted with the FTS optical axis. This was accomplished by temporarily replacing the InGaAs detector on the FTS with a second camera, which viewed the same image as the detector. The tracking camera was then aligned to view the same scene as the focal plane camera. The pointing system was directed toward sixteen targets across the LA basin with known latitude, longitude and altitude. The azimuth ($\theta_{C,i}$) and elevation ($\psi_{C,i}$) angles viewed from the CLARS site toward the sixteen targets ($i = 1-16$) were computed using

$$\theta_{C,i} = \arctan \left(\frac{\sin(\lambda_C - \lambda_{T,i}) \cos(\varphi_C - \varphi_{T,i})}{\cos(\varphi_C) \sin(\varphi_{T,i}) - \sin(\varphi_C) \cos(\varphi_{T,i}) \cos(\lambda_C - \lambda_{T,i})} \right) \quad (2)$$

$$\psi_{C,i} = \pi - \arctan \left(\frac{D_i}{Z_C - Z_{T,i}} \right) \quad (3)$$

where, λ_C and $\lambda_{T,i}$ are the longitudes of the CLARS site and target i , φ_C and $\varphi_{T,i}$ are the latitudes of the CLARS site and target i , Z_C and $Z_{T,i}$ are the altitude of the CLARS site and target i , D_i is the great circle distance between CLARS site and target i . D_i can be computed from,

$$D_i = R_E \arccos \left(\sin(\varphi_C) \sin(\varphi_{T,i}) + \cos(\varphi_C) \cos(\varphi_{T,i}) \cos(\lambda_C - \lambda_{T,i}) \right) \quad (4)$$

Los Angeles trace gas distributions from a mountaintop site

D. Fu et al.

Title Page

Abstract

Introduction

Conclusions

References

Tables

Figures

◀

▶

◀

▶

Back

Close

Full Screen / Esc

Printer-friendly Version

Interactive Discussion



where R_E is the radius of the Earth. Equations (2)–(4) assume that the Earth is spherical.

The azimuth ($\theta_{E,i}$) and elevation ($\psi_{E,i}$) angles of the gimbal's azimuth-elevation encoder for each target position, i , were fitted to the following equations to obtain the coefficients A_j :

$$\theta_{E,i} = A_1 - A_2\theta_{C,i} \quad (5)$$

$$\psi_{E,i} = A_3 - 0.5 \left\{ \psi_{C,i} - [A_4 + A_5 \sin(A_6\theta_{C,i} + A_7)] \right\} \quad (6)$$

where, $\varphi_{C,i}$ and $\psi_{C,i}$ were computed using Eqs. (2) and (3); $A_{j=1-7}$ are calibration coefficients determined from a least-squares fit to the 16 calibration targets. Using the above equations, the latitude, longitude, and elevation of any target can be used to drive the azimuth and elevation of the gimbal within its mechanical limits. After applying the pointing calibration the total uncertainty of the CLARS-FTS pointing system is 0.17° (1σ) in azimuth (about 30 % of CLARS-FTS FOV yielding a ground distance of ~ 60 m for a target that is 20 km away from CLARS) and 0.045° (1σ) in elevation (8 % of CLARS-FTS FOV yielding a ground distance of ~ 16 m for a target that is 20 km away from CLARS).

2.4 Weather station

Meteorological data are recorded at the CLARS facility. Prior to 18 December 2012, a Davis Vantage weather station was employed. It provided measurements of barometric pressure (digital accuracy ± 1.0 hPa), air temperature ($\pm 0.5^\circ\text{C}$), relative humidity ($\pm 5\%$), wind speed ($\pm 5\%$), wind direction ($\pm 5^\circ$), and precipitation ($\pm 4\%$). After this date, an R. M. Young weather system was employed to replace the Davis Vantage system that was destroyed by lightning. Sensors are mounted ~ 5 m above the CLARS container measuring barometric pressure (accuracy ± 0.3 hPa from -40°C to 60°C), air temperature ($\pm 0.3^\circ\text{C}$ from -50°C to 50°C), relative humidity ($\pm 1\%$ at 23°C), solar radiation ($\pm 5\%$ under daylight spectrum conditions), wind speed (± 0.5 m s $^{-1}$), wind

Los Angeles trace gas distributions from a mountaintop site

D. Fu et al.

Title Page

Abstract

Introduction

Conclusions

References

Tables

Figures

◀

▶

◀

▶

Back

Close

Full Screen / Esc

Printer-friendly Version

Interactive Discussion



direction ($\pm 5^\circ$), and the precipitation rate (2% up to 25 mm h^{-1} , 3% up to 50 mm h^{-1}). Real-time weather data are available online at <http://clarsweather.jpl.nasa.gov/>. The archived data are available on the Weather Underground web site (link available in the reference list).

3 Measurements using CLARS-FTS

Three operating modes are on the CLARS-FTS measurement schedule: Los Angeles Basin Surveys (LABS), Spectralon[®] Viewing Observations (SVO), and Instrument Status Evaluation Measurements (ISEM). The upper panel of Supplement Fig. 1 shows the viewing geometry of LABS and SVO. LABS and SVO are the observations that CLARS-FTS conducts daily. In LABS mode, the pointing system stares at each ground site in the Los Angeles basin and CLARS-FTS records atmospheric absorption spectra over a broad spectral range ($4000\text{--}8600 \text{ cm}^{-1}$) using reflected sunlight as the light source. SVO, provide the background level of GHG gases. In SVO, CLARS-FTS measures the greenhouse gas concentration above the CLARS site by pointing at a Spectralon[®] target on the rooftop. Since the CLARS mountaintop site is located above the boundary layer, SVO measurements give the background trace gas abundances in the free troposphere. Pointing at the Spectralon[®] plate instead of the Sun simplifies pointing system requirements by eliminating the need to track the Sun. This mode has the additional advantages of attenuating the direct solar beam intensity to levels comparable to the reflected radiance from the land targets, and also provides spectra averaged over the entire solar disk. The Spectralon[®] plate is a nearly lambertian scattering surface over the spectral range of $4000\text{--}25\,000 \text{ cm}^{-1}$ with a reflectance greater than 98.5% over the range of $6700 \text{ cm}^{-1}\text{--}25\,000 \text{ cm}^{-1}$ and 95% over the range $4000\text{--}40\,000 \text{ cm}^{-1}$. ISEM, which is conducted monthly, uses HCl gas cell measurements and IR laser measurements for verifying the alignment quality and stability. The approach was discussed in Sect. 2.2.4.

Los Angeles trace gas distributions from a mountaintop site

D. Fu et al.

Title Page

Abstract

Introduction

Conclusions

References

Tables

Figures

⏪

⏩

◀

▶

Back

Close

Full Screen / Esc

Printer-friendly Version

Interactive Discussion



**Los Angeles trace
gas distributions
from a mountaintop
site**

D. Fu et al.

Title Page

Abstract

Introduction

Conclusions

References

Tables

Figures

◀

▶

◀

▶

Back

Close

Full Screen / Esc

Printer-friendly Version

Interactive Discussion

Daily measurements from CLARS-FTS follow a pre-programmed sequence, in which the CLARS pointing system either directs light reflected from the targets in the Los Angeles basin (LABS mode) or the Spectralon® plate on the rooftop of CLARS site (SVO mode) into the spectrometer. The sequences can be changed to accommodate the needs of special observations. Supplement Table 1 lists the target coordinates, measurement mode, and descriptions of targets in a typical measurement sequence. Supplement Fig. 1 shows the location of targets over LA basin. The measurement sequence is repeated ~ 5–8 times daily.

A spectral resolution of 0.12 cm^{-1} is used in daily CLARS-FTS measurements. The typical interferometer scan time to obtain an absorption spectrum is 18 s for the maximum OPD setting of 5 cm (spectral resolution $0.6/\text{MOPD} = 0.12\text{ cm}^{-1}$, an angular radius of the circular internal field of view = 4.970 mrad , with a circular field stop of 3.03 mm in diameter) and OPD speed of 0.6 cm s^{-1} (corresponding to a mirror velocity of 0.3 cm s^{-1}). In the measurement sequence, CLARS-FTS averages 12 single scan spectra (~ 3 min measurement time) for each target site to achieve a spectral SNR of ~ 300 : 1 after co-addition. Figure 3 presents sample atmospheric absorption spectra measured using CLARS-FTS on 3 September 2012 around 10.33 a.m. local time (solar zenith angle 32.442°). The measurement was taken by targeting Santa Anita racetrack (34.141° N , 118.042° W , 155 m a.s.l., 9.3 km slant distance to CLARS site), Arcadia, California.

In the downward viewing geometry used in the CLARS-FTS measurements, the sunlight travels through the boundary layer twice: once on the way to the target and a second time from the target to CLARS. The resulting light path through the boundary layer is typically greater than 20 km which is several times longer than other commonly used viewing geometries, e.g., observing the direct solar beam from the surface, or measurement of surface-reflected sunlight from aircraft and spacecraft.

4 Data processing and error analysis

This section describes the algorithms for conversion of interferograms to spectra (Sect. 4.1), spectra to slant column densities of trace gases along the light path, (Sect. 4.2), computation of column average volume mixing ratios (Sect. 4.3) and sample retrievals for two reflection points in the LA basin (Sect. 4.4). In Sect. 4.5, the estimation of measurement uncertainties is presented.

4.1 Interferogram to spectrum

As discussed in Sect. 2.2.3, CLARS-FTS records single-sided interferograms with uniform-time sampling in both the IR and reference channels. The CLARS interferogram processing program (CLARS-IPP) converts interferograms (Level 1a data) into spectra (Level 1b data). The CLARS-IPP algorithm applies the following post-processing steps to each recorded scan: (1) converts time-domain interferogram to path-difference domain interferogram; (2) corrects for solar intensity variations (SIV); (3) corrects phase error, and (4) converts the interferogram into a spectrum using the Fast Fourier Transform (FFT) algorithm.

Conversion of the interferogram from the time domain to the path difference domain requires an accurate estimate of the instantaneous mirror velocity. This information is obtained from the reference laser interferograms. In CLARS-IPP, the algorithm that computes the instantaneous velocity was written for the Mars Atmosphere Trace Molecule Occultation Spectrometer (MATMOS) project (Pingree, et al., 2007; Bekker et al., 2008, 2009). This technique has been demonstrated in previous studies (Brasumas and Cushman, 1997; Manning and Combs, 1999; Campbell, 2008). In the original method of Brault (1996), the laser interferogram zero crossings are detected by a hardware comparator, with the intervals measured by counting pulses from a high-frequency clock triggered by the comparator. These values are used to resample the IR interferogram at constant intervals of OPD. The method used by CLARS-FTS is to

Los Angeles trace gas distributions from a mountaintop site

D. Fu et al.

Title Page

Abstract

Introduction

Conclusions

References

Tables

Figures

◀

▶

◀

▶

Back

Close

Full Screen / Esc

Printer-friendly Version

Interactive Discussion



Los Angeles trace gas distributions from a mountaintop site

D. Fu et al.

Title Page

Abstract

Introduction

Conclusions

References

Tables

Figures

⏪

⏩

◀

▶

Back

Close

Full Screen / Esc

Printer-friendly Version

Interactive Discussion



of the solar spectrum to calculate the monochromatic spectrum of light that originates from the sun, passes through the atmosphere, reflects from the Earth's surface, makes a second pass through the lower atmosphere and enters the CLARS-FTS instrument. The radiances are then processed through the CLARS-FTS instrument model to simulate the measured radiances at the appropriate spectral resolution.

GFIT uses the Voigt lineshape function and optionally includes line mixing for CO₂, CH₄ and O₂. Atmospheric absorption coefficients are calculated line-by-line for each gas in a chosen spectral window, and are used together with the assumed temperature, pressure, and VMR profiles in the forward model to calculate the atmospheric transmittance spectrum. The Voigt profile is used in the analysis of CLARS-FTS spectra. The simulated spectra were compared with measured spectra and the a priori VMR profiles are iteratively scaled to minimize the RMS differences between the calculated and measured spectra. The theoretical instrument line shape (ILS), verified by fits to low-pressure HCl gas cell lines, is used in calculating the forward model. The atmosphere is represented by 70 levels in the forward model calculation. Pressure- and temperature dependent absorption coefficients are computed for each absorption line at each level. Profiles of temperature and geopotential height are obtained from the NOAA Climate Diagnostics Center (CDC), with 17 pressure levels from 1000 to 10 hPa and 1° × 1° geographic resolution. At pressures less than 10 hPa, climatological profiles of temperature and geopotential height are used. Measured surface pressures at the LA basin weather stations are used to define the lowest model level.

The monochromatic atmospheric absorption spectrum is then multiplied by a synthetic solar spectrum which is represented by the following equation

$$I_i = S_i e^{\frac{-x_i^2}{d_i^4 + x_i^2 y_i^2}} \quad (7)$$

where, i is the index of the monochromatic wavelength grid, S_i , x_i , y_i , and d_i are the line-center optical thickness, the frequency from line center, 1/e-folding width and Doppler width in the empirical solar line list, respectively. The solar line list covers the range

4.5.1 Estimation of XGHG measurement precision

The uncertainties returned by GFIT assume a Gaussian distribution of residuals from the spectral fits. In reality, this is usually not the case due to systematic artifacts (e.g., errors/omissions in the spectroscopic data base, the modeling of the instrument response, and uncertainty in the pointing accuracy resulting in errors in the computed optical path). These can dominate the spectral fitting residuals produced by GFIT. Since these artifacts are generally the same from spectrum to spectrum, an uncertainty calculated from the RMS spectral fit generally underestimates the true precision. Hence, we utilize the differences of XGHG between two spectral regions to estimate the precisions of CLARS-FTS measurements. These differences include a systematic bias coming from variations in the spectral signatures of interfering species, and the inconsistencies between spectroscopic parameters within these spectral regions. The remaining variation (1σ standard deviation of the mean differences) is given by the equation,

$$\sigma_{\Delta XGHG} = \sqrt{\text{err}_{MW1}^2 + \text{err}_{MW2}^2 + 2\text{err}_{MW1}\text{err}_{MW2}} \quad (10)$$

where, $\sigma_{\Delta XGHG}$ is 1σ standard deviation of the mean differences using two spectral regions, err_{MW1} and err_{MW2} are the measurement uncertainties/precisions of two spectral regions. The spectral noise and the number of spectral points are the dominant factors of measurement precisions. These two factors are nearly identical between MW1 and MW2 since their small separations ($\sim 5\text{--}100\text{ cm}^{-1}$) on the measured spectra and their nearly identical widths of spectral fitting windows (Table 1). The spectral noises are random, i.e., no correlation on the spectral noise between two adjacent spectral bands. Hence, the cross term in the right hand side of Eq. (10) vanishes and Eq. (10) can be written as

$$\text{err}_{MW1} = \text{err}_{MW2} = \sigma_{\Delta XGHG} / \sqrt{2} \quad (11)$$

Table 2 lists the estimated measurement precisions of XCO₂, XCH₄, and XCO over CLARS site, Santa Anita Park and west Pasadena targets by applying Eq. (11) to the XGHG differences using two adjacent spectral regions (right panels in Figs. 7, 11, 12 and Supplement Figs. 4, 8, 11). The measurements of Spectralon[®] targets on 3 January 2013 show higher precision (XCO₂: 0.09%; XCH₄: 0.13%; XCO: 2.00%) than the measurements over Santa Anita Park (XCO₂: 0.14%; XCH₄: 0.25%; XCO: 4.01%) and west Pasadena targets (XCO₂: 0.24%; XCH₄: 0.46%; XCO: 8.01%). The measurement precision on 18 January 2013 shows characteristics similar to those on 3 January 2013. The low precision of XCO arises from the decreased spectral SNR in the spectral regions used in the measurements of CO slant column densities. The measurement precision shows target site dependence due to the differences of spectral SNR over three target sites. Overall, the high precision of CLARS-FTS measurements is sufficient to capture the diurnal variations of XCO₂, XCH₄ and XCO and the differences among different targets over LA basin.

4.5.2 Estimation of XGHG measurement accuracy

Systematic error sources include the uncertainties in spectroscopic line parameters, light path calculation uncertainties, and errors in the ILS, which affects the accuracy of CLARS-FTS measurements. Table 3 lists the estimated measurement accuracy. The uncertainties of measured XCO₂, XCH₄ and XCO arise from spectroscopic parameters, which are expected to be similar to those from previous studies (Washenfelter et al., 2006; Wunch et al., 2010, 2011). Regular HCl cell and infrared laser measurements are carried out to assess the alignment stability and performance of the FTS. The uncertainties in the light path computation arise from residual pointing errors and from the neglect of aerosol scattering in the radiative transfer calculations. As discussed previously, aerosol interference is reduced by using the simultaneously measured O₂ slant column density, which is proportional to the optical path length, to compute XGHG (Sect. 4.3).

Los Angeles trace gas distributions from a mountaintop site

D. Fu et al.

Title Page

Abstract

Introduction

Conclusions

References

Tables

Figures

⏪

⏩

◀

▶

Back

Close

Full Screen / Esc

Printer-friendly Version

Interactive Discussion



0.14% and 1.94%. For the measurements over LA basin targets (Santa Anita Park and west Pasadena), the precisions of retrieved XCO₂, XCH₄, and XCO are 0.16% and 0.22, 0.26 and 0.48%, 4.10 and 8.04%. The high measurement precisions of CLARS-FTS provide the capabilities of capturing the diurnal variations of XCO₂, XCH₄, and XCO over LA basin targets and the differences among the LA basin targets. The calibration of XCO₂, XCH₄, and XCO retrievals using aircraft in-situ profiles will be accomplished in the near future.

Supplementary material related to this article is available online at
[http://www.atmos-meas-tech-discuss.net/6/8807/2013/
amtd-6-8807-2013-supplement.pdf](http://www.atmos-meas-tech-discuss.net/6/8807/2013/amtd-6-8807-2013-supplement.pdf).

Acknowledgements. We are grateful to K. Bowman, A. Butz, R. Duren, A. Eldering, C. Frankenberg, F. Hase, E. Kort, K. F. Li, C. Miller, D. Natzic, S. Newman, C. Roehl, R. L. Shia, J. Stutz, P. Wennberg, J. Worden, D. Wunch and Y. L. Yung for many helpful discussions. Support from the NASA Instrument Incubator Program, NOAA Climate Program, NIST, California Air Resources Board and the JPL Earth Science and Technology Directorate is gratefully acknowledged. Copyright 2013, California Institute of Technology. Government sponsorship acknowledged.

References

- Bekker, D. L., Lukowiak, M., Shaaban, M., Blavier, J.-F. L., and Pingree, P. J.: A Hybrid-FPGA System for On-Board Data Processing Targeting the MATMOS FTIR Instrument, Aerospace Conference, IEEE, 1–15, doi:10.1109/AERO.2008.4526400, Big Sky, Montana, 1–8 March, 2008.
- Bekker, D. L., Blavier, J.-F. L., Toon, G. C., and Servais, C.: An FPGA-based Data Acquisition and Processing System for the MATMOS FTIR Instrument, Aerospace Conference, IEEE, 1–11, doi:10.1109/AERO.2009.4839459, Big Sky, Montana, 7–14 March, 2009.

Los Angeles trace gas distributions from a mountaintop site

D. Fu et al.

Title Page

Abstract

Introduction

Conclusions

References

Tables

Figures



Back

Close

Full Screen / Esc

Printer-friendly Version

Interactive Discussion



Los Angeles trace gas distributions from a mountaintop site

D. Fu et al.

Title Page

Abstract

Introduction

Conclusions

References

Tables

Figures

⏪

⏩

◀

▶

Back

Close

Full Screen / Esc

Printer-friendly Version

Interactive Discussion



- Bekker, D. L., Blavier, J. L., Fu, D., Key, R. W., Manatt, K. S., McKinney, C., Rider, D. M., Sander, S. P., Werne, T. A., Wu, A. C., Wu, Y. H.: Command and data handling system for the panchromatic Fourier transform spectrometer, Aerospace Conference, IEEE, 1–10, doi:10.1109/AERO.2012.6187224, Big Sky, Montana, 3–10 March, 2012.
- 5 Bergland, G.: A radix-eight fast Fourier transform subroutine for real-valued series, IEEE Trans. Audio Electroacoust., 17, 138–144, 1969.
- Brasunas, J. C. and Cushman, G. M.: Uniform time sampling Fourier transform spectroscopy, Appl. Opt., 36, doi:10.1364/AO.36.002206, 2206–2210, 1997.
- Brault, J. W.: New approach to high-precision Fourier transform spectrometer design, Appl. Opt., 35, 2891–2896, doi:10.1364/AO.35.002891, 1996.
- 10 Brault, J. W., Brown, L. R., Chackerian, C., Freedman, R., Predoi-Cross, A., Pine, A. S., Self-broadened $^{12}\text{C}^{16}\text{O}$ line shapes in the $\nu = 2 \leftarrow 0$ band, J. Mol. Spectrosc, 222, 220–239, 2003.
- Brown, L. R., Benner, D. C., Champion, J. P., Devi, V. M., Fejard, L., Gamache, R. R., Gabard, T., Hilico, J. C., Lavorel, B., Loete, M., Mellau, G. C., Nikitin, A., Pine, A. S., Predoi-Cross, A., Rinsland, C. P., Robert, O., Sams, R. L., Smith, M. A. H., Tashkun, S. A., Tyuterev, V. G.: Methane line parameters in HITRAN, J. Quant. Spectrosc. Ra., 82, 219–238, 2003.
- 15 Campbell, J.: Synthetic quadrature phase detector/demodulator for Fourier transform spectrometers, Appl. Opt., 47, 6889–6894, 2008.
- Connes, J.: Recherches sur la spectroscopie par transformation de Fourier, Rev. Opt. Théor. Instrum., 40, 45–79, 116–140, 171–190, 231–265, 1961, translated into English by Flanagna, C. A., Spectroscopic Studies Using Fourier Transform, Vol. 3157, US Naval Ordnance Test Station Technical Publication, Inoyokern, California, 1963.
- 20 Croes, B. E.: New directions: California's programs for improving air quality and minimizing greenhouse gas emissions, Atmos. Environ., 47, 562–563, doi:10.1016/j.atmosenv.2010.05.041, 2012.
- Davis, S. P., Abrams, M. C., and Brault, J. W.: Fourier Transform Spectrometry, 2nd Edn., Academic, Academic Press, San Diego, California, 2001.
- Fishman, J., Iraci, L. T., Al-Saadi, J., Chance, K., Chavez, F., Chin, M., Coble, P., Davis, C., DiGiacomo, P. M., Edwards, D., Eldering, A., Goes, J., Herman, J., Hu, C., Jacob, D., Jordan, C., Kawa, S. R., Key, R., Liu, X., Lohrenz, S., Mannino, A., Natraj, V., Neil, D., Neu, J., Newchurch, M., Pickering, K., Salisbury, J., Sosik, H., Subramaniam, A., Tzortziou, M., Wang, J., Wang, M.: The United States' next generation of atmospheric composition and coastal ecosystem measurements: NASA's Geostationary Coastal and Air Pollution Events
- 30

Los Angeles trace gas distributions from a mountaintop site

D. Fu et al.

Title Page

Abstract

Introduction

Conclusions

References

Tables

Figures

⏪

⏩

◀

▶

Back

Close

Full Screen / Esc

Printer-friendly Version

Interactive Discussion

(GEO-CAPE) mission, *B. Am. Meteorol. Soc.*, 93, 1547–1566, doi:10.1175/BAMS-D-11-00201.1, 2012.

Forman, M. L., Steel, W. H., and Vanasse, G. A.: Correction of asymmetric interferograms obtained in Fourier spectroscopy, *J. Opt. Soc. Am.*, 56, 59–63, doi:10.1364/JOSA.56.000059, 1966.

Frankenberg, C., Warneke, T., Butz, A., Aben, I., Hase, F., Spietz, P., and Brown, L. R.: Pressure broadening in the $2\nu_3$ band of methane and its implication on atmospheric retrievals, *Atmos. Chem. Phys.*, 8, 5061–5075, doi:10.5194/acp-8-5061-2008, 2008.

Fu, D., Sung, K., Boone, C. D., Walker, K. A., Bernath, P. F.: Ground-based solar absorption studies for the Carbon Cycle science by Fourier Transform Spectroscopy (CC-FTS) mission, *J. Quant. Spectrosc. Ra.*, 109, 2219–2243, 2008.

Geller, M.: A high resolution atlas of the infrared spectrum of the Sun and the Earth atmosphere from space, vol. III, Key to identification of solar features from 650 to 4800 cm^{-1} ; NASA Reference Publication 122; NASA: Washington, DC, USA, 1992.

Geller, M.: Line identification in ATMOS solar spectra, in: Laboratory and Astronomical High Resolution Spectra, Proceedings of ASP Conference No. 81, Brussels, Belgium, 29 August–2 September 1994, ASP Conference Series, edited by: Sauval, A. J., Blomme, R., and Grevesse, N., Astronomical Society of the Pacific, San Francisco, CA, USA, 81, 1995.

Griesmann, U., Kling, R., Burnett, J. H., and Bratasz, L.: The NIST FT700 Vacuum Ultraviolet Fourier Transform Spectrometer: applications in ultraviolet spectrometry and radiometry, *Proc. SPIE*, 3818, 180–188, 1999.

Griffiths, P. R., De Haseth, J. A.: *Fourier Transform Infrared Spectrometry*, 2nd edn., Wiley-Interscience, New York, 2007.

Gordon, I. E., Kass, S., Campargue, A., Toon, G. C.: First identification of the $\mathbf{a}^1\Delta_g - \mathbf{X}^3\Sigma_g^-$ electric quadrupole transitions of oxygen in solar and laboratory spectra, *J. Quant. Spectrosc. Ra.*, 111, 1174–1183, 2010.

Hase, F., Blumenstock, T., and Paton-Walsh, C.: Analysis of instrumental line shape of high-resolution FTIR-spectrometers using gas cell measurements and a new retrieval software, *Appl. Opt.*, 38, 3417–3422, 1999.

Hornweg, D., Freire, M., Lee, M. J., Bhada-Tata, P., Yuen, B.: *Cities and Climate Change: An Urgent Agenda*, The World Bank, Washington, D.C., 2010.

Irion, F. W., Gunson, M. R., Toon, G. C., Chang, A. Y., Eldering, A., Mahieu, E., Manney, G. L., Michelsen, H. A., Moyer, E. J., Newchurch, M. J., Osterman, G. B., Rinsland, C. P., Salaw-

Los Angeles trace gas distributions from a mountaintop site

D. Fu et al.

Title Page

Abstract

Introduction

Conclusions

References

Tables

Figures

◀

▶

◀

▶

Back

Close

Full Screen / Esc

Printer-friendly Version

Interactive Discussion



itch, R. J., Sen, B., Yung, Y. L., and Zander, R.: Atmospheric Trace Molecule Spectroscopy (ATMOS) Experiment Version 3 data retrievals, *Appl. Opt.*, 41, 6968–6979, 2002.

Jenouvrier, A., Daumont, L., Regalia-Jarlot, L., Tyuterev, V. G., Carleer, M., Vandaele, A. C., Mikhailenko, S., and Fally, S.: Fourier transform measurements of water vapor line parameters in the 4200–6600 cm^{-1} region, *J. Quant. Spectrosc. Ra.*, 105, 326–355, doi:10.1016/j.jqsrt.2006.11.007, 2007.

Keppel-Aleks, G., Toon, G. C., Wennberg, P. O., and Deutscher, N. M.: Reducing the impact of source brightness fluctuations on spectra obtained by Fourier-transform spectrometry, *Appl. Opt.*, 46, 4774–4779, doi:10.1364/AO.46.004774, 2007.

Key, R., Sander, S., Eldering, A., Rider, D., Blavier, J.-F., Bekker, D., Wu, Y.-H., Manatt, K.: The Geostationary Fourier Transform Spectrometer, *Aerospace Conference Proceedings, IEEE*, doi:10.1109/AERO.2012.6187164, Big Sky, Montana, 3–10 March, 2012.

Kort, E. A., Frankenberg, C., Miller, C. E., and Oda, T.: Space-based observations of megacity carbon dioxide, *Geophys. Res. Lett.*, 39, L17806, doi:10.1029/2012GL052738, 2012.

Livingston, W. and Wallace, L.: An atlas of the solar spectrum in the infrared from 1850 to 9000 cm^{-1} (1.1 to 5.4 μm), NSO Technical Report, NSO, Tucson, AZ, USA, 1991.

McKain, K., Wofsy, S. C., Nehrkorn, T., Eluszkiewicz, J., Ehleringer, J. R., and Stephens, B. B.: Assessment of ground-based atmospheric observations for verification of greenhouse gas emissions from an urban region, *P. Natl. Acad. Sci. USA*, 109, 8423–8428, doi:10.1073/pnas.1116645109, 2012.

Manning, C. J. and Combs, R. J.: FT-IR Interferogram sampling validation and correction, *Proc. SPIE*, 3537, 181–186, 1999.

National Research Council, Committee on Earth Science and Applications from Space: A community assessment and strategy for the future: Earth science and applications from space: national imperatives for the next decade and beyond, National Academies Press, Washington, D.C., 2007.

Newman, S. M., Lane, I. C., Orr-Ewing, A. J., Newnham, D. A., and Ballard, J.: Integrated absorption intensity and Einstein coefficients for the $\text{O}_2 \text{ a}^1\Delta_g - \text{X}^3\Sigma_g^- (0,0)$ transition: a comparison of cavity ring down and high resolution Fourier transform spectroscopy with a long-path absorption cell, *J. Chem. Phys.* 110, 10749–10757, doi:10.1063/1.479018, 1999.

Norton, R. H. and Rinsland, C. P.: ATMOS data processing and science analysis methods, *Appl. Opt.*, 30, 389–400, 1991.

Los Angeles trace gas distributions from a mountaintop site

D. Fu et al.

Title Page

Abstract

Introduction

Conclusions

References

Tables

Figures

◀

▶

◀

▶

Back

Close

Full Screen / Esc

Printer-friendly Version

Interactive Discussion

- O'Dell, C. W., Connor, B., Bösch, H., O'Brien, D., Frankenberg, C., Castano, R., Christi, M., Eldering, D., Fisher, B., Gunson, M., McDuffie, J., Miller, C. E., Natraj, V., Oyafuso, F., Polonsky, I., Smyth, M., Taylor, T., Toon, G. C., Wennberg, P. O., and Wunch, D.: The ACOS CO₂ retrieval algorithm – Part 1: Description and validation against synthetic observations, *Atmos. Meas. Tech.*, 5, 99–121, doi:10.5194/amt-5-99-2012, 2012.
- Olsen, S. C. and Randerson, J. T.: Differences between surface and column atmospheric CO₂ and implications for carbon cycle research, *J. Geophys. Res.*, 109, D02301, doi:10.1029/2003JD003968, 2004.
- Pingree, P. J., Blavier, J.-F. L., Toon, G. C., and Bekker, D. L.: An FPGA/SoC approach to on-board data processing enabling new Mars science with smart payloads, *Aerospace Conference Proceedings, IEEE*, Vol. 1, 1–12, doi:10.1109/AERO.2007.353091, Big Sky, Montana, 3–10 March, 2007.
- Pougatchev, N. S., Campbell, J. F., Regan, C. R., Abrams, M. C., Brault, J. W., Farmer, C. B., and Hinton, D. E.: Advanced technologies high resolution Fourier transform spectrometer for atmospheric studies, *Aerospace Conference Proceedings, IEEE*, Vol. 3, 237–243, doi:10.1109/AERO.2000.879851, Big Sky, Montana, 18–25 March, 2000.
- Rothman, L. S., Gordon I. E., Barbe, A., Benner, C. D., Bernath, P. F., Birk, M., Boudon, V., Brown, L. R., Campargue, A., Champion, J.-P., Chance, K., Coudert, L. H., Dana, V., Devi, V. M., Fally, S., Flaud, J.-M., Gamache, R. R., Goldman, A., Jacquemart, D., Kleiner, I., Lacombe, N., Lafferty, W. J., Mandin, J.-Y., Massie, S. T., Mikhailenko, S. N., Miller, C. E., Moazzen-Ahmadi, N., Naumenko, O. V., Nikitin, A. V., Orphal, J., Perevalov, V.I., Perrin, A., Predoi-Cross, A., Rinsland, C. P., Rotger, M., Šimevřková, M., Smith, M. A. H., Sung, K., Tashkun, S. A., Tennyson, J., Toth, R. A., Vandaele, A. C., and Vander Auwera, J.: The HITRAN 2008 molecular spectroscopic database, *J. Quant. Spectrosc. Ra.*, 110, 533–572, 2009.
- Sen, B., Osterman, G. B., Salawitch, R. J., Toon, G. C., Margitan, J. J., Blavier, J.-F., Chang, A. Y., May, R. D., Webster, C. R., Stimpfle, R. M., Bonne, G. P., Voss, P. B., Perkins, K. K., Anderson, J. G., Cohen, R. C., Elkins, J. W., Dutton, G. S., Hurst, D. F., Romashkin, P. A., Atlas, E. L., Schauffler, S. M., and Loewenstein, M.: The budget and partitioning of stratospheric chlorine during the 1997 Arctic summer, *J. Geophys. Res.*, 104, 26653–26665, 1999.

**Los Angeles trace
gas distributions
from a mountaintop
site**D. Fu et al.

Title Page

Abstract

Introduction

Conclusions

References

Tables

Figures

◀

▶

◀

▶

Back

Close

Full Screen / Esc

Printer-friendly Version

Interactive Discussion

- Smith, K. M. and Newnham, D. A.: Near-infrared absorption cross sections and integrated absorption intensities of molecular oxygen (O_2 , O_2-O_2 , and O_2-N_2), *J. Geophys. Res.*, 105, 7383–7396, 2000.
- Toth, R. A.: Line positions and strengths of N_2O between 3515 and 7800 cm^{-1} , *J. Mol. Spectrosc.*, 197, 158–87, 1999.
- Toth, R. A.: N_2 and air-broadened linewidths and frequency-shifts of N_2O , *J. Quant. Spectrosc. Ra.*, 66, 285–304, 2000.
- Toth, R. A.: Measurements of positions, strengths and self-broadened widths of H_2O from 2900 to 8000 cm^{-1} : line strength analysis of the 2nd triad bands, *J. Quant. Spectrosc. Ra.*, 94, 51–107, 2005.
- Toth, R. A., Brown, L. R., Miller, C. E., Malathy Devi, V., and Benner, D. C.: Spectroscopic database of CO_2 line parameters: 4300–7000 cm^{-1} , *J. Quant. Spectrosc. Ra.*, 109, 906–921, doi:10.1016/j.jqsrt.2007.12.004, 2008.
- Yang, Z., Wennberg, P. O., Cageao, R. P., Pongetti, T. J., Toon, G. C., Sander, S. P.: Ground-based photon path measurements from solar absorption spectra of the O_2 A-band, *J. Quant. Spectrosc. Ra.*, 90, 309–321, doi:10.1016/j.jqsrt.2004.03.020, 2005.
- Wallace, L., Hinkle, K., Livingston, W. C.: An Atlas of the Photospheric Spectrum from 8900 to 13 600 cm^{-1} (7350 to 11 230 Å), NSO Technical Report, NSO, Tucson, AZ, USA, 1993.
- Washenfelder, R. A., Toon, G. C., Blavier, J. F., Yang, Z., Allen, N. T., Wennberg, P. O., Vay, S. A., Matross, D. M., and Daube, B. C.: Carbon dioxide column abundances at the Wisconsin Tall Tower site, *J. Geophys. Res.* 111, D22305, doi:10.1029/2006JD007154, 2006.
- Weather Underground web site: <http://www.wunderground.com/weatherstation/> (last access: 30 September 2013), 2013
- Wunch, D., Wennberg, P. O., Toon, G. C., Keppel-Aleks, G., and Yavin, Y. G.: Emissions of greenhouse gases from a North American megacity, *Geophys. Res. Lett.*, 36, L15810, doi:10.1029/2009GL039825, 2009.
- Wunch, D., Toon, G. C., Wennberg, P. O., Wofsy, S. C., Stephens, B. B., Fischer, M. L., Uchino, O., Abshire, J. B., Bernath, P., Biraud, S. C., Blavier, J.-F. L., Boone, C., Bowman, K. P., Browell, E. V., Campos, T., Connor, B. J., Daube, B. C., Deutscher, N. M., Diao, M., Elkins, J. W., Gerbig, C., Gottlieb, E., Griffith, D. W. T., Hurst, D. F., Jiménez, R., Keppel-Aleks, G., Kort, E. A., Macatangay, R., Machida, T., Matsueda, H., Moore, F., Morino, I., Park, S., Robinson, J., Roehl, C. M., Sawa, Y., Sherlock, V., Sweeney, C., Tanaka, T., and

Zondlo, M. A.: Calibration of the Total Carbon Column Observing Network using aircraft profile data, *Atmos. Meas. Tech.*, 3, 1351–1362, doi:10.5194/amt-3-1351-2010, 2010.

Wunch, D., Toon, G. C., Blavier, J.-F. L., Washenfelder, R. A., Notholt, J., Connor, B. J., Griffith, D. W. T., Sherlock, V., and Wennberg, P. O.: The total carbon column observing network,

5 *Philos. T. Roy. Soc. A*, 369, 2087–2112, doi:10.1098/rsta.2010.0240, 2011.

AMTD

6, 8807–8854, 2013

Los Angeles trace gas distributions from a mountaintop site

D. Fu et al.

Title Page

Abstract

Introduction

Conclusions

References

Tables

Figures

◀

▶

◀

▶

Back

Close

Full Screen / Esc

Printer-friendly Version

Interactive Discussion

Table 1. Spectral range, species that have spectral signatures within the spectral range, and sources of spectroscopic parameters used in spectral fittings.

Spectral Range cm ⁻¹	(source of spectroscopic line parameters) ^e Gases to Fit	Auxiliary Parameters to fit
6180.0–6260.0	^f CO ₂ , ^g H ₂ O, ^g HDO, ^{h,i} CH ₄	cl ^a ct ^b fs ^c
6297.0–6382.0	^f CO ₂ , ^g H ₂ O, ^g HDO	cl ct fs
4810.0–4890.0	^f CO ₂ , ^j N ₂ O, ^g H ₂ O, ^g HDO, ^k CH ₄ , ^l CO	cl ct fs
5880.0–5996.0	^{h,i} CH ₄ , ^f CO ₂ , ^g H ₂ O, ^g HDO	DLPBF ^d
6007.0–6145.0	^{h,i} CH ₄ , ^f CO ₂ , ^g H ₂ O, ^g HDO	DLPBF
4208.7–4257.3	^l CO, ^k CH ₄ , ^g H ₂ O, ^g HDO	cl ct fs
4262.0–4318.8	^l CO, ^k CH ₄ , ^g H ₂ O, ^g HDO	DLPBF
7765.0–8005.0	^m O ₂ , ⁿ O ₂ , ^g H ₂ O	cl ct fs

^a Continuum level.^b Continuum tilt.^c Frequency shift.^d Fitting the continuum level using Discrete Legendre Polynomial Basis Functions (DLPBF).^e All of the spectroscopic parameters are available in HITRAN 2008 compilation prepared by Rothman et al. (2009).^f Toth et al. (2008).^g Toth (2005) with the addition (in 2005-7) of hundreds of weak H₂O lines that are visible in humid, high-airmass TCCON spectra. Jenouvrier et al. (2007) subsequently identified many of these weak lines.^h GFIT (Feb 2013 version) includes the weak CH₄ lines extending from 6180 to 6220 cm⁻¹ which were provided by Linda Brown.ⁱ Frankenberg et al. (2008).^j Toth (1999, 2000).^k Brown et al. (2003).^l Brault et al. (2003).^m Line list created by Andrew Orr-Ewing using the PGOPHER code, based on lab measurements of Newman et al. (1999). The widths were subsequently modified to be 1.5% larger than those in Yang et al. (2005) in order to minimize the airmass dependence of retrieved O₂ column density, as described by Washenfelder et al. (2006). O₂ quadrupoles lines are from Gordon et al. (2010).ⁿ The collision induced absorption (CIA) is represented by a pseudo-linelist based on fits to lab spectra described by Smith and Newnham (2000). The CIA is not used in the determination of the O₂ column. It is fitted only to minimize its impact on the discrete O₂ lines.

Los Angeles trace gas distributions from a mountaintop site

D. Fu et al.

Title Page

Abstract

Introduction

Conclusions

References

Tables

Figures

◀

▶

◀

▶

Back

Close

Full Screen / Esc

Printer-friendly Version

Interactive Discussion

Los Angeles trace gas distributions from a mountaintop site

D. Fu et al.

Title Page

Abstract

Introduction

Conclusions

References

Tables

Figures

⏪

⏩

◀

▶

Back

Close

Full Screen / Esc

Printer-friendly Version

Interactive Discussion



Table 3. Estimated measurement accuracy¹.

Error Sources	XCO ₂	XCH ₄	XCO
Spectroscopic Line Parameters, Pressure, Temperature Profiles ²	~ 1.1 %	~ 4.0 %	~ 2.0 %
Light path calculation ³	< 1.0 %	< 1.0 %	< 1.0 %
Instrument line shape ⁴	< 1.0 %	< 1.0 %	< 1.0 %
Uncertainty Priori to Calibration	< 3.1 %	< 6.0 %	< 4.0 %

¹ The uncertainty was estimated prior to the CLARS-FTS calibration/validation activity. The discussion of measurement accuracy estimation is introduced in Sect. 4.5.2.

² Estimation was made based on the uncertainty of TCCON measurements prior to applying calibration factors (Wunch et al., 2010, 2011).

³ Refer to the measured XGHG uncertainty arise from the remaining impacts of aerosol that were not removed by the approach of computing XGHG in Sect. 4.3.

⁴ Refer to the differences between measured and theoretical line shape functions in Sect. 2.2.4.

Los Angeles trace gas distributions from a mountaintop site

D. Fu et al.

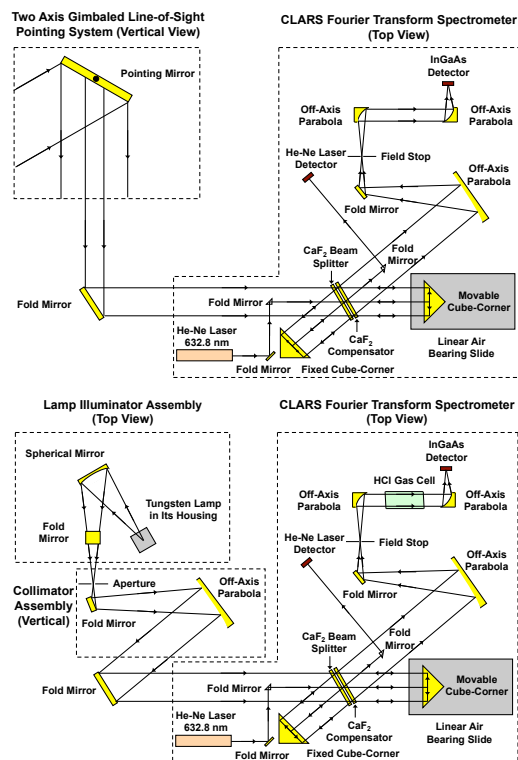


Fig. 1. Optical layouts of California Laboratory for Atmospheric Remote Sensing Fourier Transform Spectrometer (CLARS-FTS) for measuring greenhouse gases (top panel), and gas cell spectra to verify instrument alignment quality and stability (bottom panel). The core is a Michelson-type interferometer using cube-corner retro reflectors. It covers a spectral range of 4000 to 15000 cm^{-1} with a maximum optical path difference (MOPD) of 30 cm (or spectral resolution of 0.02 cm^{-1}).

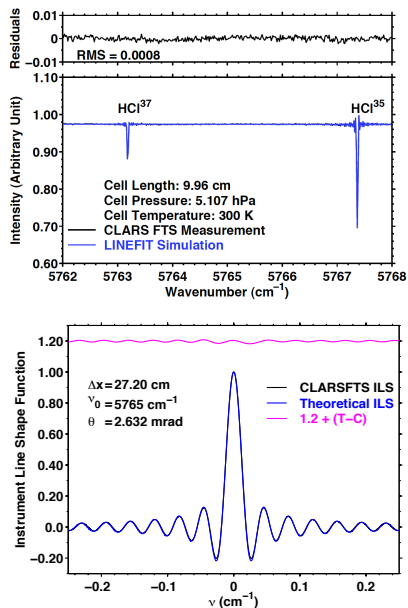


Fig. 2. Top panel: HCl gas cell spectra near 5765 cm^{-1} measured by CLARS-FTS (black curve) and simulated by LINEFIT program (blue curve); Bottom panel: instrument line shape functions (ILS) of CLARS-FTS (black line) and an ideal FTS (blue line); the differences between theoretical ILS and CLARS-FTS ILS (magenta line; it was offset by 1.2 for clarity). The spectral fitting residuals (top panel) were normalized by the continuum level of measured HCl cell spectra. The root mean square of spectral fitting residual was 0.08% of spectral continuum level. The following parameters were used in both measurements and simulation: an optical path difference = 27.2 cm, an angular radius of the circular internal field of view = 2.632 mrad, HCl cell length = 9.96 cm, gas cell total pressure = 5.107 hPa, HCl gas pressure in the cell = 5.107 hPa, cell temperature = 300 K. The symmetric ILS indicated the high quality of CLARS-FTS alignment. The full width half maximum (FWHM) of CLARS-FTS ILS is 0.022 cm^{-1} .

Los Angeles trace gas distributions from a mountaintop site

D. Fu et al.

Discussion Paper | Discussion Paper | Discussion Paper | Discussion Paper | Discussion Paper

Title Page

Abstract Introduction

Conclusions References

Tables Figures

◀ ▶

◀ ▶

Back Close

Full Screen / Esc

Printer-friendly Version

Interactive Discussion



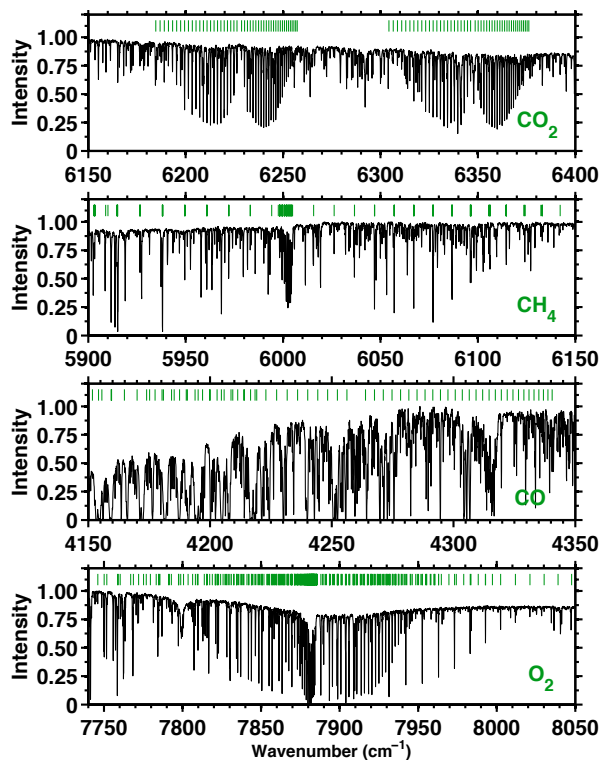


Fig. 3. Atmospheric absorption spectra measured using CLARS-FTS with a spectral resolution of 0.12 cm^{-1} on 3 September 2012. The measurement was taken by targeting at the land surface of Santa Anita racetrack (34.141° N , 118.042° W , 155 m a.s.l. , 9.3 km slant distance to CLARS site), Arcadia, California. The green vertical bars indicate the spectral line positions of target gases of interests. The spectra were coadded using 12 single scan spectra centered at 10.33 a.m. local time (solar zenith angle 32.442°) with total measurement time about 3 min. The spectral signal to noise ratio (SNR) is 420 : 1.

Los Angeles trace gas distributions from a mountaintop site

D. Fu et al.

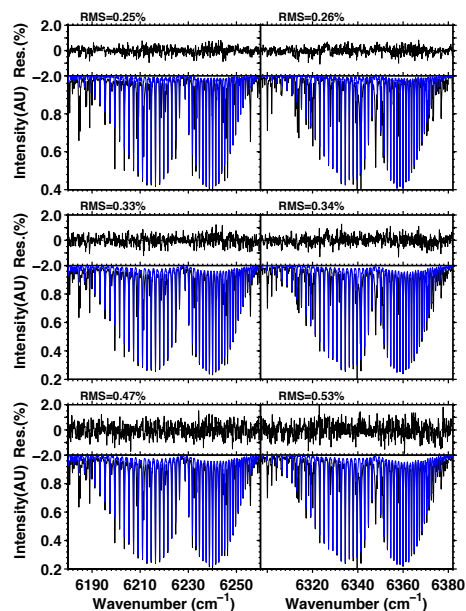


Fig. 4. Sample spectral fittings of CO₂ bands near 1.6 μm region using the CLARS-FTS measurements in the Spectralon® viewing geometry (top panels); pointing at the Santa Anita Race Track, Arcadia (middle panels); or pointing at the west Pasadena (bottom panels). The measurements were taken on 3 January 2013 with a Solar Zenith Angle (SZA) of 58.62° (top panels), 58.39° (middle panels), and 57.89° (bottom panels) respectively. Each spectrum is from 12 co-added scans, which were taken consecutively over 3 min. The spectral SNR are 532 : 1, 417 : 1, and 227 : 1 from top to bottom panels, respectively. The measured radiances subtracting the simulated spectra, which included contributions of all trace gases and solar lines, yield the spectral fitting residuals. In all panels, black curves are measured spectra and blue curves are the estimated contribution of CO₂ absorption from the spectral fittings. Contributions of other species in these spectral regions are not shown.

Title Page

Abstract

Introduction

Conclusions

References

Tables

Figures

◀

▶

◀

▶

Back

Close

Full Screen / Esc

Printer-friendly Version

Interactive Discussion

Los Angeles trace gas distributions from a mountaintop site

D. Fu et al.

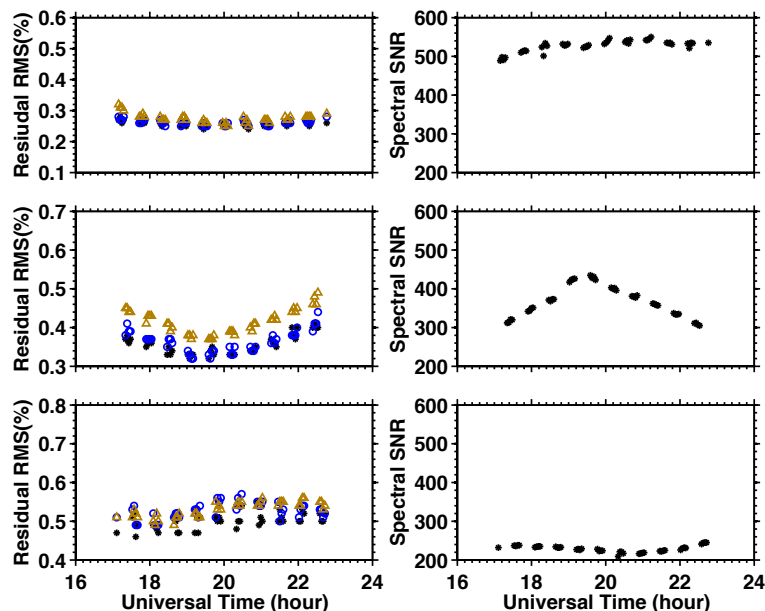


Fig. 5. Root Mean Square (RMS) of spectral fitting residuals (Left panels) and spectral SNR (right panels) as a function of time for the measurements of CO₂ and O₂ column densities in Spectralon® viewing geometry (top panels); over the Arcadia Race Track (middle panels); over west Pasadena (bottom panels). Three spectral bands centered at 6220 cm⁻¹ (black stars, noted as MW6220 thereafter), 6339 cm⁻¹ (blue circles, noted as MW6339 thereafter) and 7885 cm⁻¹ (gold triangles, noted as MW7885 thereafter) are presented, respectively. The spectral SNR were nearly identical over the three spectral bands in a measured spectrum, but varies among spectra. The measurements were performed on 3 January 2013. The spectral fitting residuals were normalized by the spectral continuum levels prior to the computation of RMS values. The spectral fitting residuals were dominated by the photon shot noise. The Chi-squared tests of spectral fitting residuals yielded values generally within 1.3.

Los Angeles trace gas distributions from a mountaintop site

D. Fu et al.

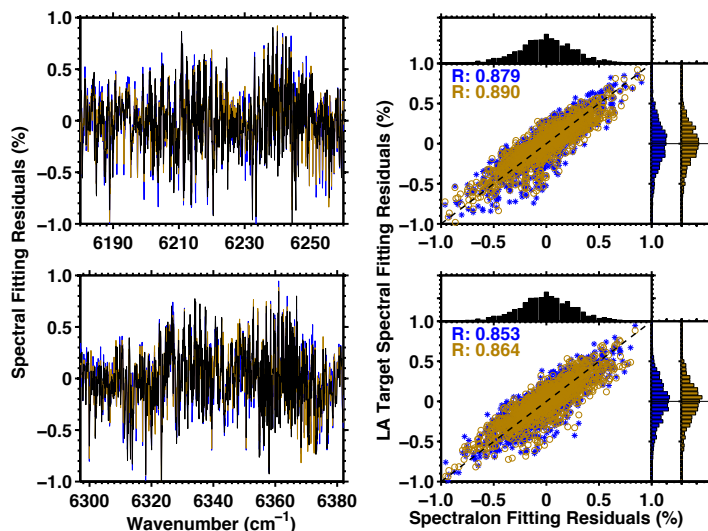


Fig. 6. The spectral fitting residuals (left panels) and their correlation, Pearson correlation coefficients (R), and histograms (right panels) with MW6220 (top panels) and MW6339 (bottom panels) for CO_2 slant column density measurements. In left panels, black curve is for Spectralon[®] viewing geometry; blue curve is for west Pasadena; gold curve is for Arcadia Race Track. In right panels, blue stars are the correlation between Spectralon[®] and west Pasadena; gold circles are the correlation between Spectralon[®] and Arcadia Race Track; the black dash lines indicate the one to one correlation. The spectral fitting residuals were generated using the co-addition of residuals of 41 spectral fittings of Spectralon[®] target, 41 spectral fittings of west Pasadena target, and 40 spectral fits of Arcadia Race Track target on 3 January 2013. The systematic residuals arise from the imperfect line shape function and spectroscopic parameters in addition to uncertainties of atmospheric pressure and temperature parameters since the magnitude and positions of spiky fitting residuals consistently appear in all three target scenes. However, the magnitude of most of systematic fitting residuals is within 0.5 % of spectral continuum levels.

Title Page

Abstract

Introduction

Conclusions

References

Tables

Figures

◀

▶

◀

▶

Back

Close

Full Screen / Esc

Printer-friendly Version

Interactive Discussion

Los Angeles trace gas distributions from a mountaintop site

D. Fu et al.

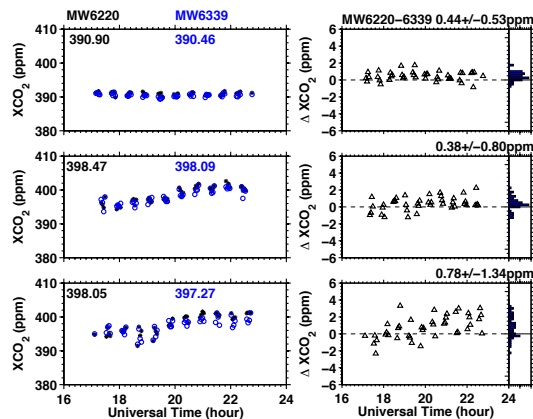


Fig. 7. XCO_2 (in parts per million, ppm) measured by CLARS-FTS with MW6220 (black dots) and MW6339 (blue circles) on 3 January 2013 (left panels) and differences of retrieved XCO_2 between the two spectral regions and the histograms (right panels) in the Spectralon[®] viewing geometry (top panels), towards the Arcadia Race Track (middle panels); and towards west Pasadena (bottom panels). Black stars in left panels: XCO_2 obtained using the spectral region of MW6220. Compared to the background levels of XCO_2 (top panels), XCO_2 over Arcadia Race Track (middle panels) and west Pasadena (bottom panels) show higher values (mean ART-SV: 7.60 ppm; mean WP-SV: 6.98 ppm) and present stronger diurnal cycles than those measurements over CLARS site. The XCO_2 values retrieved from MW6220 are higher than those of MW6339. The mean differences between MW6220 and MW6339 are 0.44 ppm, 0.38 ppm, 0.78 ppm for DSV, ART and WP respectively. It was also appeared in the spectral analyses of the TCCON measurements (~ 0.15 ppm). Both CLARS-FTS and TCCON results, which are using HITRAN 2008 line list, show improvements on the band-to-band consistency of XCO_2 , compared to those of using HITRAN 2004 line list such as Fig. 6 of Washenfelder et al. (2006) with the XCO_2 using MW6220 about 0.9 ppm higher than that of MW6339. These systematic differences of retrieved XCO_2 values between two spectral bands likely arise from the discrepancies of spectroscopic parameters between two spectral bands and the amount/intensity of spectral features of interfering species.

Title Page

Abstract

Introduction

Conclusions

References

Tables

Figures

◀

▶

◀

▶

Back

Close

Full Screen / Esc

Printer-friendly Version

Interactive Discussion

Los Angeles trace gas distributions from a mountaintop site

D. Fu et al.

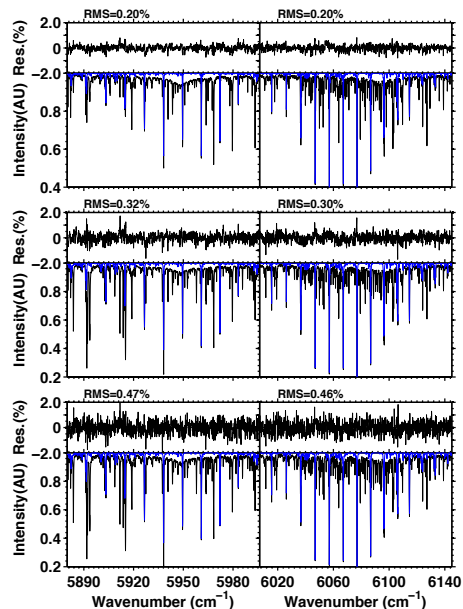


Fig. 8. Sample spectral fittings of CH_4 bands, which are centered at 5938 cm^{-1} (noted as MW5938 thereafter) and 6076 cm^{-1} (noted as MW6076 thereafter) using the CLARS-FTS measurements in the Spectralon[®] viewing geometry (top panels); pointing at the Santa Anita Race Track, Arcadia (middle panels); or pointing at the west Pasadena (bottom panels). The measurements were taken on 3 January 2013 with a Solar Zenith Angle (SZA) of 58.62° (top panels), 58.39° (middle panels), and 57.89° (bottom panels) respectively. Each spectrum is from 12 co-added scans, which were taken consecutively over 3 min. The spectral SNR are 532 : 1, 417 : 1, and 227 : 1 from top to bottom panels, respectively. The measured radiances subtracting the simulated spectra, which included contributions of all trace gases and solar lines, yield the spectral fitting residuals. In all panels, black curves are measured spectra and blue curves are the estimated contribution of CH_4 absorption from the spectral fittings. Contributions of other species in these spectral regions are not shown.

[Title Page](#)
[Abstract](#)
[Introduction](#)
[Conclusions](#)
[References](#)
[Tables](#)
[Figures](#)
[◀](#)
[▶](#)
[◀](#)
[▶](#)
[Back](#)
[Close](#)
[Full Screen / Esc](#)
[Printer-friendly Version](#)
[Interactive Discussion](#)

Los Angeles trace gas distributions from a mountaintop site

D. Fu et al.

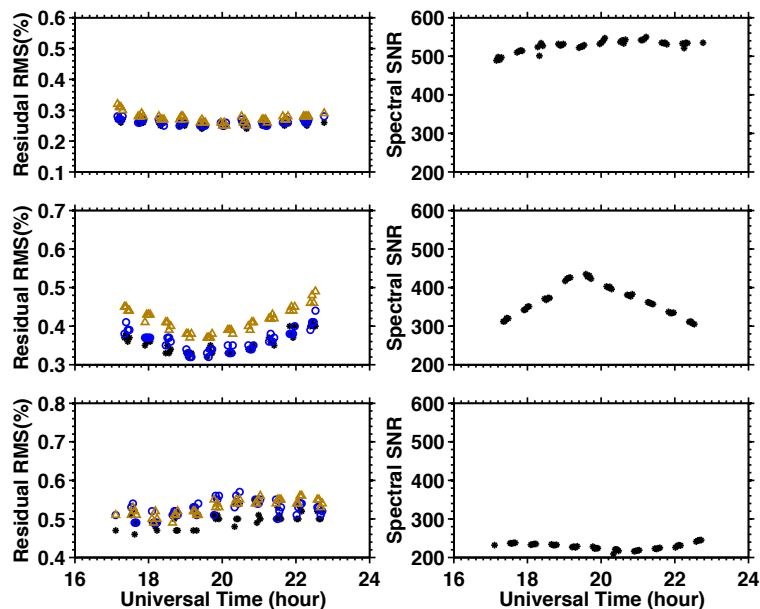


Fig. 9. Root Mean Square (RMS) of spectral fitting residuals (left panels) and spectral SNR (right panels) as a function of time for the measurements of CH_4 and O_2 column densities in Spectralon® viewing geometry (top panels); over the Arcadia Race Track (middle panels); over west Pasadena (bottom panels). Three spectral bands centered at 5938 cm^{-1} (black stars, noted as MW5938 thereafter), 6076 cm^{-1} (blue circles, noted as MW6076 thereafter) and 7885 cm^{-1} (gold triangles, noted as MW7885 thereafter) are presented, respectively. The spectral SNR were nearly identical over the three spectral bands in a measured spectrum, but varies among spectra. The measurements were performed on 3 January 2013. The spectral fitting residuals were normalized by the spectral continuum levels prior to the computation of RMS values. The spectral fitting residuals were dominated by the photon shot noise. The Chi-squared tests of spectral fitting residuals yielded values generally within 1.3.

Title Page

Abstract Introduction

Conclusions References

Tables Figures

◀ ▶

◀ ▶

Back Close

Full Screen / Esc

Printer-friendly Version

Interactive Discussion

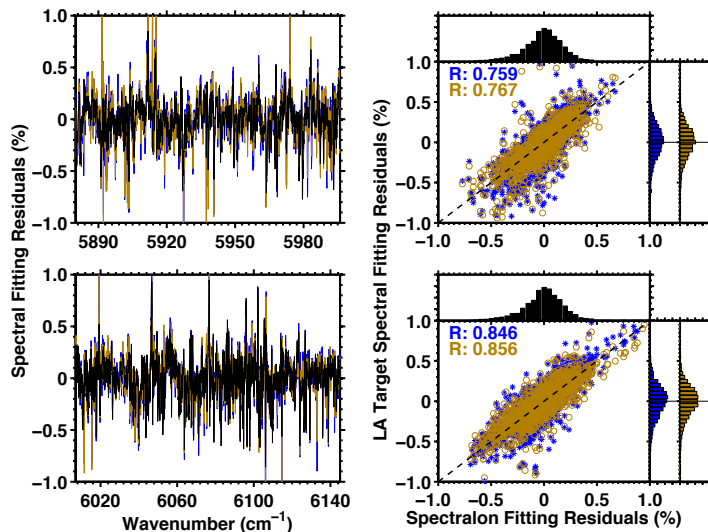


Fig. 10. The spectral fitting residuals (left panels) and their correlation, Pearson correlation coefficients (R), and histograms (right panels) with MW5938 (top panels) and MW6076 (bottom panels) for CH_4 slant column density measurements. In left panels, black curve is for Spectralon[®] viewing geometry; blue curve is for west Pasadena; gold curve is for Arcadia Race Track. In right panels, blue stars are the correlation between Spectralon[®] and west Pasadena; gold circles are the correlation between Spectralon[®] and Arcadia Race Track; the black dash lines indicate the one to one correlation. The spectral fitting residuals were generated using the co-addition of residuals of 41 spectral fittings of Spectralon[®] target, 41 spectral fittings of west Pasadena target, and 40 spectral fits of Arcadia Race Track target on 3 January 2013. The systematic residuals arise from the imperfect line shape function and spectroscopic parameters in addition to uncertainties in atmospheric pressure and temperature parameters since the magnitude and positions of spiky fitting residuals consistently appear in all three target scenes. However, the magnitude of most of systematic fitting residuals is within 0.5 % of spectral continuum levels.

Los Angeles trace gas distributions from a mountaintop site

D. Fu et al.

Title Page

Abstract Introduction

Conclusions References

Tables Figures

◀ ▶

◀ ▶

Back Close

Full Screen / Esc

Printer-friendly Version

Interactive Discussion



Los Angeles trace gas distributions from a mountaintop site

D. Fu et al.

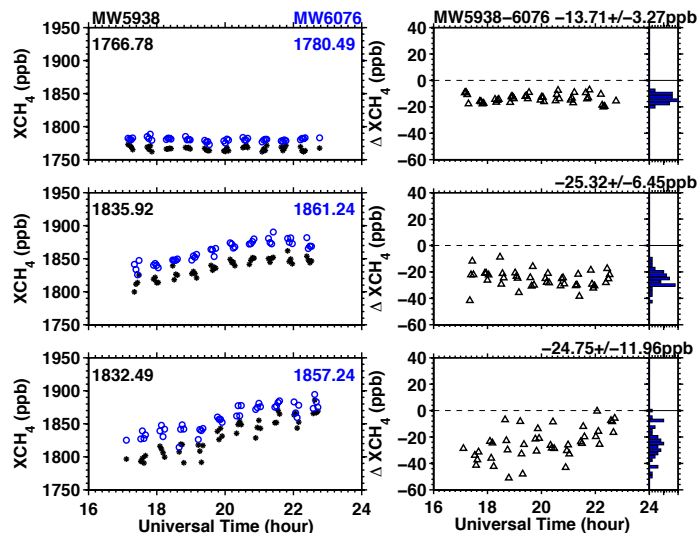


Fig. 11. XCH₄ (in parts per billion, ppb) measured by CLARS-FTS with MW5938 (black dots) and MW6076 (blue circles) on 3 January 2013 (left panels) and differences of retrieved XCH₄ between the two spectral regions and the histograms (right panels) in the Spectralon[®] viewing geometry (top panels), towards the Arcadia Race Track (middle panels); and towards west Pasadena (bottom panels). Black stars in left panels: XCH₄ obtained using the spectral region of MW5938. Compared to the background levels of XCH₄ (top panels), XCH₄ over Arcadia Race Track (middle panels) and west Pasadena (bottom panels) show higher values (mean ART-SV: 74.95 ppb; mean WP-SV: 71.23 ppb) and present stronger diurnal cycles than those measurements over CLARS site. The XCH₄ values retrieved from MW6076 are higher than those of MW5938. The mean differences between MW6076 and MW5938 are 13.71 ppb, 25.32 ppb, and 24.75 ppb for SV, ART and WP respectively. These systematic differences of retrieved XCH₄ values between two spectral bands likely arise from the discrepancies of spectroscopic parameters between two spectral bands and the amount/intensity of spectral features of interfering species.

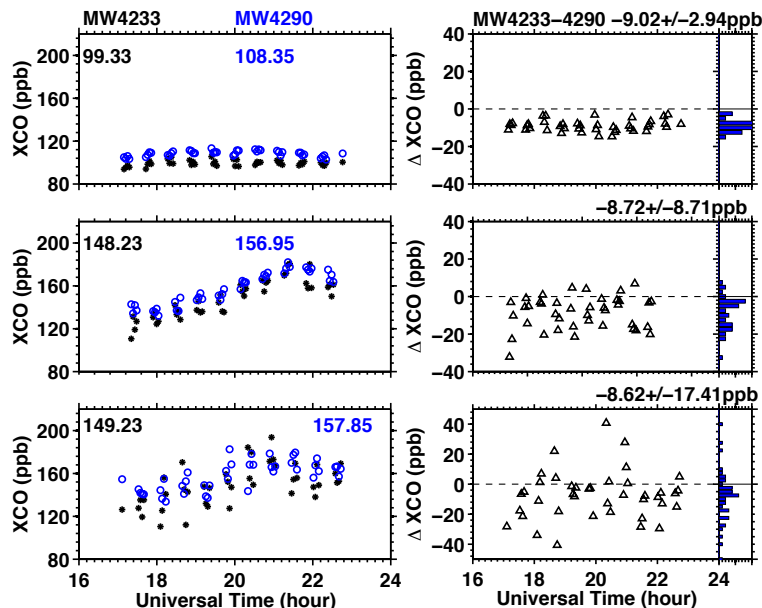


Fig. 12. XCO (in parts per billion, ppb) measured by CLARS-FTS with MW4233 (black dots) and MW4290 (blue circles) on 3 January 2013 (left panels) and differences of retrieved XCO between the two spectral regions and the histograms (right panels) in the Spectralon® viewing geometry (top panels), towards the Arcadia Race Track (middle panels); and towards west Pasadena (bottom panels). Compared to the background levels of XCO (top panels), XCO over Arcadia Race Track (middle panels) and west Pasadena (bottom panels) show higher values (mean ART-DSV: 48.75 ppb; mean WP-DSV: 49.70 ppb) and present stronger diurnal cycles than those measurements over CLARS site. The XCO values retrieved from MW4290 are higher than those of MW4233. The mean differences between MW4290 and MW4233 are 9.02 ppb, 8.72 ppb, 8.62 ppb for DSV, ART and WP respectively. These systematic differences of retrieved XCO values between two spectral bands are likely arisen from the discrepancies of spectroscopic parameters between two spectral bands and the amount/intensity of spectral features of interfering species.

Los Angeles trace gas distributions from a mountaintop site

D. Fu et al.

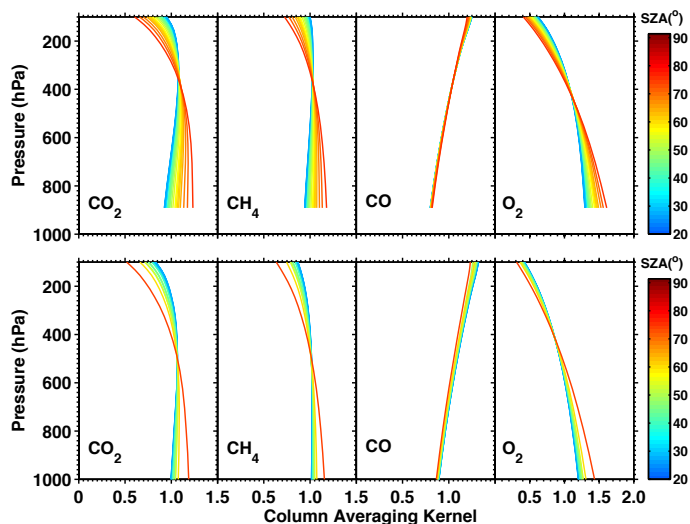


Fig. 13. Column averaging kernels of GHG measurements using CLARS-FTS with a Maximum Optical Path Difference (MOPD) of 5 cm. Top panels: for the measurements over CLARS site in the Spectralon[®] viewing geometry; bottom panels: for the measurements targeting the land surface of Arcadia race track (34.141° N, 118.042° W, 155 m a.s.l., 9.3 km slant distance to CLARS site), Arcadia, California.

Title Page

Abstract

Introduction

Conclusions

References

Tables

Figures

⏪

⏩

◀

▶

Back

Close

Full Screen / Esc

Printer-friendly Version

Interactive Discussion